

A Unified Framework for Uncertainty-Aware Explainable Artificial Intelligence: A Case Study in Power Quality Disturbance Classification

Yinsong Chen

School of Engineering, Deakin University, Melbourne, 3216, VIC, Australia

Samson S. Yu*

School of Engineering, Deakin University, Melbourne, 3216, VIC, Australia

Zhong Li

Faculty of Mathematics and Computer Science, FernUniversität in Hagen, 58084, Germany

Chee Peng Lim

Department of Computing Technologies, Swinburne University of Technology, Hawthorn, 3122, VIC, Australia

Abstract

Post-hoc explainable AI (XAI) methods typically produce deterministic attribution maps, whereas Bayesian neural networks (BNNs) induce a distribution over explanations. Capturing the variability of this distribution is important for uncertainty-aware decision-making. This paper formalises the *explanation distribution* as the push-forward measure of the BNN posterior through any Lipschitz-continuous attribution operator. It further proposes the uncertainty-aware relevance attribution operator (UA-RAO), a general family of operators that summarises the explanation distribution using the mean, variance, coefficient of variation, quantiles, and set-theoretic aggregation measures. Theoretical support is provided through Monte Carlo ac-

*Corresponding author

Email addresses: yinsong.chen@deakin.edu.au (Yinsong Chen), samson.yu@deakin.edu.au (Samson S. Yu), zhong.li@fernuni-hagen.de (Zhong Li), cplim@swin.edu.au (Chee Peng Lim)

cessibility and Wasserstein approximation bounds. The framework is evaluated on a 15-class power quality disturbance (PQD) classification benchmark, comparing three BNN approximations paired with three attribution operators using relevance mass accuracy and intersection-over-union as localisation metrics. Results show that deep ensembles with the mean UA-RAO improve localisation over the deterministic baseline, while other UA-RAO summaries reveal uncertainty patterns absent from point-estimate attributions. Qualitative results on measured signals further suggest that these patterns generalise beyond the synthetic training distribution. The framework is domain-agnostic and can be applied to any BNN paired with a Lipschitz-continuous attribution operator.

Keywords:

Bayesian neural network, explainable artificial intelligence, uncertainty quantification, power quality disturbances

1. Introduction

Deep learning has improved classification performance in safety-critical domains, such as medical imaging, fault diagnosis, and energy systems, by learning rich representations directly from raw data [1, 2]. Yet the internal decision logic of deep neural networks (DNNs) remains opaque to end users, creating what is commonly termed the *black-box problem* [1]. This opacity limits deployment in safety-critical settings where predictions must be audited, contested, or verified against domain knowledge. Regulatory frameworks such as the European Union’s General Data Protection Regulation [3] further require that automated decisions be interpretable, intensifying demand for principled transparency mechanisms. Critically, such mechanisms must also account for the uncertainty inherent in model predictions: an explanation that is itself unreliable offers limited assurance to practitioners who must act on it.

Explainable artificial intelligence (XAI) addresses this by producing post-hoc attribution maps that identify which input features drive a model’s prediction [4, 5]. Methods in this class include occlusion sensitivity, Gradient-weighted Class Activation Mapping (Grad-CAM), Local Interpretable Model-agnostic Explanations (LIME), Layer-wise Relevance Propagation (LRP), and SHapley Additive exPlanations (SHAP) [2]. These methods are now well taxonomised [1, 6] and widely deployed across scientific and engineer-

ing domains. However, virtually all are deterministic: they return a single explanation for a fixed model and fixed input. This design implicitly treats the model as a point estimate, an assumption that is invalid when the model represents inherent predictive uncertainty.

Bayesian neural networks (BNNs) address prediction uncertainty at its source by maintaining a distribution over model parameters, enabling principled separation of epistemic and aleatoric uncertainty [7, 8]. This distributional view is particularly valuable in the presence of noisy inputs, distribution shift, or ambiguous composite patterns. This introduces a new challenge for XAI: each posterior sample induces a different attribution map, making the explanation itself a random variable. Applying a deterministic XAI method to a single posterior sample, or to a point estimate of a BNN, discards this variability entirely, potentially reporting high-confidence explanations for fundamentally uncertain predictions [9, 10]. Despite their joint relevance to trustworthy machine learning, no existing framework systematically characterises the explanation itself as a statistical object whose distribution can be formally defined and bounded [11].

Several targeted approaches have begun to address this gap. Some works adapt a specific XAI operator to the Bayesian setting: Bykov et al. [9] extended LRP to BNNs (B-LRP) to propagate posterior uncertainty into saliency maps, Peltola [12] adapted LIME to Bayesian predictive distributions via Kullback–Leibler projections, and Wood et al. [11] introduced entropy-based permutation importance measures for uncertainty-aware models. Others treat the explanation as a distributional object: Bykov et al. [13] formalised the notion of an explanation distribution induced by BNN posterior sampling, Clare et al. [14] showed that distributional attribution substantially improves trustworthiness in geophysical prediction, and Mulye and Valdenegro-Toro [10] demonstrated that gradient-based explanations exhibit substantial variance across ensemble members, undermining reliance on point-estimate attributions. Each of these contributions, however, addresses a specific method–model pair or application domain. The question this paper addresses is therefore: given an arbitrary BNN posterior approximation and an arbitrary attribution operator, how can one formally define, characterise, and summarise the resulting distribution of explanations within a single probabilistic framework?

Power quality disturbance (PQD) classification provides a compelling case study for such a framework. PQD events (e.g., sags, swells, harmonics, flicker, and transients) arise from nonlinear loads, power-electronic devices,

and growing renewable integration [15], and can trigger failures in sensitive equipment and undermine grid reliability. Deep convolutional neural networks (CNNs) now dominate this task, with accuracy exceeding 98% on standard benchmarks [16], trained on large synthetic datasets spanning 15 disturbance categories [17]. However, safety-critical operation demands more than accuracy: predictions must carry calibrated confidence, particularly for composite or out-of-distribution disturbances, and explanations must be verifiable against known physical signal characteristics [18]. The combination of a well-defined 15-class taxonomy, established synthetic benchmarks, and the simultaneous need for reliable uncertainty and interpretable attribution makes PQD classification an ideal validation domain.

This paper proposes a unified uncertainty-aware explainable framework that addresses these requirements. We formalise the *explanation distribution* as the push-forward measure induced by the BNN posterior through any Lipschitz-continuous XAI operator, and introduce the *uncertainty-aware relevance attribution operator* (UA-RAO) to summarise this distribution via its mean, variance, coefficient of variation, quantiles, and set-theoretic aggregations. The framework is supported by two theoretical results: a Monte Carlo accessibility guarantee for explanation distributions (**Proposition 3.1**) and a Wasserstein approximation bound relating explanation quality to the BNN approximation gap (**Proposition 3.2**). We validate the framework on the 15-class XPQRS PQD benchmark [15], comparing three BNN approximations (deep ensemble, Laplace approximation, and Monte Carlo (MC) Dropout) paired with three XAI operators (Occlusion, Grad-CAM, and LIME) and measuring localisation fidelity via relevance mass accuracy (RMA) and intersection-over-union (IoU). The contributions of this paper are as follows:

- A unified uncertainty-aware explainable AI framework, in the sense that a single push-forward formalism covers any combination of BNN posterior approximation and Lipschitz-continuous attribution operator, enabling systematic propagation of predictive uncertainty into the explanation space without modifying either component.
- A measure-theoretic formalisation of explanation distributions for BNNs that is consistent with existing Bayesian XAI approaches and provides a unifying perspective under the push-forward formalism.
- The UA-RAO, a general operator family converting an explanation distribution into interpretable uncertainty-aware attribution maps via

multiple summary statistics, including mean, variance, coefficient of variation, quantiles, and set-theoretic aggregations.

- Theoretical guarantees on Monte Carlo estimation of explanation distributions (**Proposition 3.1**) and on Wasserstein error propagation from BNN approximation to explanation quality (**Proposition 3.2**).
- An empirical evaluation on a 15-class synthetic PQD benchmark, comparing three BNN approximations and three XAI operators using localisation metrics, together with a qualitative assessment on real-world measured sag events, demonstrating improved localisation fidelity over deterministic baselines and revealing explanation uncertainty patterns that point-estimate attributions do not expose.

The remainder of this paper is organised as follows. Section 2 introduces the necessary background, covering the PQD classification problem, Bayesian neural network formulations, and the XAI operators considered. Section 3 presents the unified framework, formalising explanation distributions as push-forward measures and introducing the UA-RAO together with its theoretical guarantees. Section 4 describes the evaluation framework, including ground-truth disturbance segmentation, point-explanation localisation metrics, and distributional assessment criteria. Section 5 reports experimental results on the 15-class synthetic PQD benchmark and includes a qualitative assessment on real-world measured data. Section 6 concludes the paper.

2. Preliminaries

This section establishes the prerequisites for the framework in Section 3. The three subsections introduce, respectively, the PQD classification setting, the Bayesian neural network formulation with approximate inference, and the local relevance attribution operator—the three components that the framework combines.

2.1. Power Quality Disturbance Classification

Let $x[n] \in \mathbb{R}$ denote a discrete-time voltage waveform of length N ($n = 1, \dots, N$) sampled from a power network operating at nominal frequency. The undisturbed reference signal is modelled as a pure sinusoid,

$$x_0[n] = A \sin(\omega n + \phi), n = 1, \dots, N, \quad (1)$$

where A , ω , and ϕ represent the amplitude, angular frequency, and phase, respectively. A *simple disturbance* refers to a local deviation of x from x_0 attributable to a single physical event (e.g., sag, transient). A *complex disturbance* arises from the superposition or concatenation of $k > 1$ simple events. In this work, 15 representative PQD categories are considered, covering both simple and complex disturbance types, as listed in [16].

Dataset Formulation. Each raw waveform $x[n]$ with fixed length N is treated as a univariate time series. Let $\mathcal{X} \subseteq \mathbb{R}^N$ denote the input space and $\mathcal{Y} = \{1, 2, \dots, M\}$ the label space. A labelled PQD dataset can be represented by

$$\mathcal{D} = \{(x^{(i)}, y^{(i)})\}_{i=1}^{N_{\mathcal{D}}}, \quad x^{(i)} \in \mathcal{X}, y^{(i)} \in \mathcal{Y}, \quad (2)$$

where $N_{\mathcal{D}}$ is the number of samples in the dataset.

Deep Learning Classifier. The PQD classifier is a parametric function

$$f_{\theta} : \mathcal{X} \rightarrow \Delta^{M-1}, \quad (3)$$

where $\Delta^{M-1} = \{p \in \mathbb{R}^M : p_m \geq 0, \sum_m p_m = 1\}$ is the $(M-1)$ -simplex. The output $f_{\theta}(x) \in \Delta^{M-1}$ is a probability vector over the M classes, and the predicted label is $\hat{y} = \arg \max_m [f_{\theta}(x)]_m$. The parameters θ are estimated by minimising the categorical cross-entropy loss over \mathcal{D} ,

$$\mathcal{L}(\theta) = -\frac{1}{|\mathcal{D}|} \sum_{(x,y) \in \mathcal{D}} \sum_{m=1}^M \mathbf{1}[y = m] \log[f_{\theta}(x)]_m, \quad (4)$$

with $\mathbf{1}[\cdot]$ the indicator function. A one-dimensional convolutional neural network (1D-CNN) is adopted as the backbone, as its hierarchical feature extraction is well suited to the time-localised and morphologically distinct signatures of PQDs.

2.2. Bayesian Neural Network

Deterministic classifiers f_{θ} provide point predictions without quantifying predictive confidence. In safety-critical applications such as power quality monitoring, distinguishing reliable predictions from uncertain ones is essential. To this end, the classifier is formulated as a BNN by imposing a prior distribution $p(\theta)$ over the model parameters. Given the training set \mathcal{D} , Bayesian inference yields the posterior

$$p(\theta | \mathcal{D}) = \frac{p(\mathcal{D} | \theta) p(\theta)}{p(\mathcal{D})}, \quad (5)$$

where

$$p(\mathcal{D} | \theta) = \prod_{(x,y) \in \mathcal{D}} p(y | x, \theta) \quad (6)$$

is the discriminative likelihood, and

$$p(\mathcal{D}) = \int_{\Theta} p(\mathcal{D} | \theta) p(\theta) d\theta \quad (7)$$

is the evidence. For a new input x , the posterior predictive distribution, which captures epistemic uncertainty, is obtained by marginalising over the parameter posterior,

$$p(y | x, \mathcal{D}) = \int_{\Theta} p(y | x, \theta) p(\theta | \mathcal{D}) d\theta. \quad (8)$$

Approximate Posterior Inference Since the exact posterior $p(\theta | \mathcal{D})$ is generally intractable for DNNs, an approximate posterior $q_{\phi}(\theta)$, parameterised by ϕ , is introduced [7] such that

$$q_{\phi}(\theta) \approx p(\theta | \mathcal{D}). \quad (9)$$

The predictive distribution is correspondingly approximated as

$$p(y|x, \mathcal{D}) \approx \int_{\Theta} p(y|x, \theta) q_{\phi}(\theta) d\theta. \quad (10)$$

Since this integral is generally intractable, it is estimated using Monte Carlo integration. Given S samples $\theta^{(s)} \sim q_{\phi}(\theta)$, $s = 1, \dots, S$,

$$p(y|x, \mathcal{D}) \approx \frac{1}{S} \sum_{s=1}^S p(y|x, \theta^{(s)}). \quad (11)$$

By the law of large numbers, this estimator converges asymptotically to the predictive distribution,

$$\lim_{S \rightarrow \infty} \frac{1}{S} \sum_{s=1}^S p(y|x, \theta^{(s)}) = p(y|x, \mathcal{D}). \quad (12)$$

This Monte Carlo estimator is the computational basis on which the explanation distribution in Section 3 is made tractable.

2.3. Explainable Artificial Intelligence

XAI methods are generally divided into *global* and *local* approaches. *Global* methods characterise model behaviour over entire datasets, whereas *local* methods attribute the relevance of individual predictions to specific input features through a relevance attribution operation [13]. This study focuses exclusively on *local* XAI methods, which are well suited to PQD classification because they provide instance-specific interpretations essential for validating individual decisions in safety-critical power systems.

Relevance Attribution Operator. Let f_θ denote the classifier under parameter realisation θ . A *local* relevance attribution operator is defined as

$$\mathcal{T}_{x,\theta}[f_\theta](x) = R_\theta(x), \quad (13)$$

where $R_\theta(x) \in \mathbb{R}^N$ is a time-aligned saliency signal. The component $R_\theta(x)[n]$ quantifies the influence of $x[n]$ on the classifier decision under parameter realisation θ .

3. A Unified Framework for Uncertainty-Aware Explainable Artificial Intelligence

Section 2 established the framework prerequisites: the approximate posterior q_ϕ over network parameters, and the local relevance attribution operator $\mathcal{T}_{x,\theta}[f_\theta]$ that maps any parameter realisation to a saliency signal (Section 2.3). The shorthand $\tau_x(\theta) = \mathcal{T}_{x,\theta}[f_\theta](x)$ is adopted below for compactness. This section formalises the distribution these objects jointly induce over explanations, establishes its theoretical properties, and introduces the UA-RAO as a general summarisation operator.

3.1. Explanation Distribution

Under the Bayesian formulation, θ is distributed according to $q_\phi(\theta)$. Consequently, for any fixed input x , parameter uncertainty induces a distribution over the explanations $R_\theta(x)$.

Notation. Throughout this section, q_ϕ denotes a probability measure on $(\Theta, \mathcal{B}(\Theta))$. In the common variational-inference setting, q_ϕ admits a Lebesgue density, also written $q_\phi(\theta)$, so that $dq_\phi(\theta) = q_\phi(\theta) d\theta$. Both notations are used interchangeably whenever the density exists. All integrals are otherwise stated in the Lebesgue–Stieltjes sense.

Definition 3.1 (Explanation Distribution). Let $q_\phi(\theta)$ be the approximate parameter posterior and $\tau_x: \Theta \rightarrow \mathbb{R}^N$ the attribution map defined above. The *explanation distribution* at input x is the push-forward measure $p_{q_\phi}(\cdot | x, \mathcal{D}) := (\tau_x)_\# q_\phi$ on $(\mathbb{R}^N, \mathcal{B}(\mathbb{R}^N))$, defined by

$$p_{q_\phi}(A | x, \mathcal{D}) = q_\phi(\tau_x^{-1}(A)) = \int_{\Theta} \mathbf{1}[\tau_x(\theta) \in A] dq_\phi(\theta), \quad A \in \mathcal{B}(\mathbb{R}^N), \quad (14)$$

where $\mathcal{B}(\mathbb{R}^N)$ is the Borel σ -algebra on \mathbb{R}^N .

Assumption 3.1 (Continuity of the Attribution Operator). *The map $\tau_x: \Theta \rightarrow \mathbb{R}^N$, $\tau_x(\theta) = \mathcal{T}_{x,\theta}[f_\theta](x)$, is continuous on Θ w.r.t. the parameter-space norm $\|\cdot\|_2$.*

Under **Assumption 3.1**, τ_x is Borel-measurable, since every continuous map between metric spaces is Borel-measurable [19]. Hence $\tau_x^{-1}(A) \in \mathcal{B}(\Theta)$ for every $A \in \mathcal{B}(\mathbb{R}^N)$, the integral in Eq. (14) is well-defined under q_ϕ , and $p_{q_\phi}(\cdot | x, \mathcal{D})$ is a valid probability measure on $(\mathbb{R}^N, \mathcal{B}(\mathbb{R}^N))$.

Remark 3.1 (Measure-Theoretic Interpretation). **Definition 3.1** defines the explanation distribution as a push-forward probability measure rather than as a density. Specifically, for any Borel set $A \subseteq \mathbb{R}^N$, $p_{q_\phi}(A | x, \mathcal{D})$ denotes the probability that the attribution map $\tau_x(\theta)$ falls in A when $\theta \sim q_\phi$. This formulation is general and does not require the induced distribution to admit a Lebesgue density.

Assumption 3.1 is mild in the sense that continuity of f_θ in θ , which holds for standard architectures with continuous activation functions, is sufficient to ensure it for most local XAI methods.

The following proposition shows that any statistic expressible as an expectation of a q_ϕ -integrable function γ is accessible by Monte Carlo integration from $p_{q_\phi}(\cdot | x, \mathcal{D})$.

Proposition 3.1 (Monte Carlo Accessibility of the Approximate Explanation Distribution). *Let **Assumption 3.1** hold, and let $p_{q_\phi}(\cdot | x, \mathcal{D})$ be the explanation distribution in **Definition 3.1**. Let $\gamma: \mathbb{R}^N \rightarrow \mathbb{R}^d$, $d \geq 1$, be Borel-measurable and satisfy*

$$\mathbb{E}_{\theta \sim q_\phi} [\|\gamma(\tau_x(\theta))\|_2] < \infty. \quad (15)$$

For i.i.d. samples $\{\theta^{(s)}\}_{s=1}^S \sim q_\phi$, define $R^{(s)}(x) := \tau_x(\theta^{(s)})$. Then,

$$\frac{1}{S} \sum_{s=1}^S \gamma(R^{(s)}(x)) \xrightarrow{a.s.} \mathbb{E}_{R \sim p_{q_\phi}(\cdot | x, \mathcal{D})} [\gamma(R)] \quad \text{as } S \rightarrow \infty. \quad (16)$$

Proof. The proof has three steps.

Step 1. By **Assumption 3.1**, τ_x is Borel-measurable. Hence, for any $A \in \mathcal{B}(\mathbb{R}^N)$,

$$P(R^{(s)}(x) \in A) = P(\theta^{(s)} \in \tau_x^{-1}(A)) = q_\phi(\tau_x^{-1}(A)) = p_{q_\phi}(A | x, \mathcal{D}),$$

where the last equality follows from Eq. (14). Therefore, each $R^{(s)}(x)$ follows $p_{q_\phi}(\cdot | x, \mathcal{D})$ [20]. Since $R^{(s)}(x) = \tau_x(\theta^{(s)})$ is a measurable function of $\theta^{(s)}$ and $\{\theta^{(s)}\}_{s=1}^S$ are i.i.d., the sequence $\{R^{(s)}(x)\}_{s=1}^S$ is also i.i.d. [21].

Step 2. By the push-forward identity [19],

$$\mathbb{E}_{R \sim p_{q_\phi}(\cdot | x, \mathcal{D})}[\gamma(R)] = \int_{\mathbb{R}^N} \gamma(r) dp_{q_\phi}(r | x, \mathcal{D}) = \int_{\Theta} \gamma(\tau_x(\theta)) dq_\phi(\theta) = \mathbb{E}_{\theta \sim q_\phi}[\gamma(\tau_x(\theta))]. \quad (17)$$

Applying the same identity to the nonnegative measurable function $\|\gamma(\cdot)\|_2$ and using Eq. (15) show that γ is integrable w.r.t. $p_{q_\phi}(\cdot | x, \mathcal{D})$.

Step 3. Let $Z_s := \gamma(R^{(s)}(x))$. By Step 1, $\{Z_s\}$ are i.i.d. random vectors in \mathbb{R}^d , and Eq. (15) implies $\mathbb{E}[\|Z_1\|_2] < \infty$. For each coordinate $j \in \{1, \dots, d\}$, the scalar sequence $\{(Z_s)_j\}$ is i.i.d. and satisfies $\mathbb{E}[|(Z_1)_j|] \leq \mathbb{E}[\|Z_1\|_2] < \infty$. Kolmogorov's strong law of large numbers [21] therefore gives $(1/S) \sum_{s=1}^S (Z_s)_j \xrightarrow{a.s.} \mathbb{E}[(Z_1)_j]$. Since $d < \infty$, coordinate-wise almost-sure convergence implies almost-sure convergence in \mathbb{R}^d : for each coordinate j the exceptional null set \mathcal{N}_j satisfies $P(\mathcal{N}_j) = 0$, so their finite union $\bigcup_{j=1}^d \mathcal{N}_j$ is also a null set [20]. Combining this result with Eq. (17) yields

$$\frac{1}{S} \sum_{s=1}^S \gamma(R^{(s)}(x)) \xrightarrow{a.s.} \mathbb{E}_{\theta \sim q_\phi}[\gamma(\tau_x(\theta))] = \mathbb{E}_{R \sim p_{q_\phi}(\cdot | x, \mathcal{D})}[\gamma(R)],$$

which proves Eq. (16). □

To bound the error introduced by the approximate posterior, we impose the following stronger regularity condition.

Assumption 3.2 (Lipschitz Continuity of the Attribution Map). *There exists a finite constant $L_{\tau_x} > 0$ such that*

$$\|\tau_x(\theta) - \tau_x(\theta')\|_2 \leq L_{\tau_x} \|\theta - \theta'\|_2, \quad \forall \theta, \theta' \in \Theta.$$

Assumption 3.2 strengthens **Assumption 3.1**, since Lipschitz continuity implies continuity.

Remark 3.2 (Applicability of **Assumption 3.2** to the Tested XAI Operators). *Occlusion* replaces contiguous waveform segments with a constant and queries f_θ . Since f_θ is Lipschitz in θ under standard weight-norm bounds, τ_x inherits Lipschitz continuity with L_{τ_x} proportional to the window length and the network’s global Lipschitz constant. *Grad-CAM* computes gradient-weighted spatial averages of feature maps. It is piecewise linear in θ and is Lipschitz on each linear region, so **Assumption 3.2** holds almost everywhere. *LIME* introduces additional randomness through its perturbation sampling step, making $\tau_x(\theta)$ stochastic in the LIME-internal sense. Therefore, **Proposition 3.2** applies to the conditional expectation of the LIME attribution given θ , and the Lipschitz constant is inherited from the surrogate fitting procedure. Verifying tight numerical values of L_{τ_x} for specific architectures is left to future work.

Proposition 3.2 (Approximation Error of the Explanation Distribution). *Let Assumption 3.2 hold. Define the ideal explanation distribution as the push-forward of the true posterior,*

$$p(\cdot \mid x, \mathcal{D}) := (\tau_x)_\# p(\theta \mid \mathcal{D}),$$

and let

$$p_{q_\phi}(\cdot \mid x, \mathcal{D}) := (\tau_x)_\# q_\phi.$$

Assume that $p(\theta \mid \mathcal{D})$ and q_ϕ have finite first moments on $(\Theta, \|\cdot\|_2)$. Then, for every 1-Lipschitz function $\gamma : \mathbb{R}^N \rightarrow \mathbb{R}$,

$$\left| \mathbb{E}_{R \sim p(\cdot \mid x, \mathcal{D})}[\gamma(R)] - \mathbb{E}_{R \sim p_{q_\phi}(\cdot \mid x, \mathcal{D})}[\gamma(R)] \right| \leq L_{\tau_x} W_1(p(\theta \mid \mathcal{D}), q_\phi), \quad (18)$$

where W_1 denotes the Wasserstein-1 distance.

Proof. The proof has two steps.

Step 1. We first show the stability of W_1 under the push-forward map τ_x . Let π be any coupling of $p(\theta \mid \mathcal{D})$ and q_ϕ , and define

$$\hat{\pi} := (\tau_x \times \tau_x)_\# \pi.$$

Then $\hat{\pi}$ is a coupling of $p(\cdot | x, \mathcal{D})$ and $p_{q_\phi}(\cdot | x, \mathcal{D})$. Therefore,

$$\begin{aligned} W_1(p(\cdot | x, \mathcal{D}), p_{q_\phi}(\cdot | x, \mathcal{D})) &\leq \int_{\mathbb{R}^N \times \mathbb{R}^N} \|r - r'\|_2 \hat{\pi}(dr, dr') \\ &= \int_{\Theta \times \Theta} \|\tau_x(\theta) - \tau_x(\theta')\|_2 \pi(d\theta, d\theta') \\ &\leq L_{\tau_x} \int_{\Theta \times \Theta} \|\theta - \theta'\|_2 \pi(d\theta, d\theta'). \end{aligned}$$

Taking the infimum over all couplings π gives

$$W_1(p(\cdot | x, \mathcal{D}), p_{q_\phi}(\cdot | x, \mathcal{D})) \leq L_{\tau_x} W_1(p(\theta | \mathcal{D}), q_\phi). \quad (19)$$

Step 2. The finite first-moment assumption on $p(\theta | \mathcal{D})$ and q_ϕ , together with the Lipschitz continuity of τ_x , implies that both push-forward measures have finite first moments on \mathbb{R}^N . Hence, by Kantorovich–Rubinstein duality, for any 1-Lipschitz function $\gamma : \mathbb{R}^N \rightarrow \mathbb{R}$,

$$\left| \mathbb{E}_{R \sim p(\cdot | x, \mathcal{D})}[\gamma(R)] - \mathbb{E}_{R \sim p_{q_\phi}(\cdot | x, \mathcal{D})}[\gamma(R)] \right| \leq W_1(p(\cdot | x, \mathcal{D}), p_{q_\phi}(\cdot | x, \mathcal{D})).$$

Combining this inequality with Eq. (19) proves Eq. (18). \square

Remark 3.3 (Interpretation of the Approximation Error Bound). The bound in Eq. (18) identifies two factors governing the approximation error. The term $W_1(p(\theta | \mathcal{D}), q_\phi)$ measures the discrepancy between the approximate and true posteriors in parameter space, while L_{τ_x} quantifies how sensitively the attribution map propagates this discrepancy into explanation space. Consequently, if $W_1(p(\theta | \mathcal{D}), q_\phi) \rightarrow 0$, then

$$W_1(p_{q_\phi}(\cdot | x, \mathcal{D}), p(\cdot | x, \mathcal{D})) \rightarrow 0,$$

and hence $p_{q_\phi}(\cdot | x, \mathcal{D})$ converges weakly to $p(\cdot | x, \mathcal{D})$. The convergence rate is controlled by the posterior approximation error and modulated by the Lipschitz constant L_{τ_x} . In practice, $W_1(p(\theta | \mathcal{D}), q_\phi)$ is intractable for high-dimensional θ . Practical surrogates include the evidence lower bound (ELBO) gap $\text{KL}(q_\phi \| p(\theta | \mathcal{D}))$ from variation inference, sliced Wasserstein distances on low-dimensional projections of θ , and the predictive calibration error as an indirect measure for approximation quality.

3.2. Uncertainty-Aware Relevance Attribution Operator

Monte Carlo accessibility of the explanation distribution (**Proposition 3.1**) enables practical computation of the UA-RAO, a general operator mapping $p_{q_\phi}(\cdot | x, \mathcal{D})$ to uncertainty-aware explanation summaries. Throughout this subsection, the attribution operator is understood to explain a fixed target class c . In applications c can be specified by the user or set to $c = \arg \max_m p_{q_\phi}(y = m | x, \mathcal{D})$.

Definition 3.2 (Uncertainty-Aware Relevance Attribution Operator). Let q_ϕ be the approximate posterior and let τ_x satisfy **Assumption 3.1**, so that $p_{q_\phi}(\cdot | x, \mathcal{D}) = (\tau_x)_\# q_\phi$ is a well-defined probability measure on $(\mathbb{R}^N, \mathcal{B}(\mathbb{R}^N))$. For any Borel-measurable functional

$$\Phi: \mathcal{P}(\mathbb{R}^N) \rightarrow \mathcal{Y}_\Phi,$$

where $\mathcal{P}(\mathbb{R}^N)$ is the space of probability measures on $(\mathbb{R}^N, \mathcal{B}(\mathbb{R}^N))$ and \mathcal{Y}_Φ is the output space of the chosen summary (e.g. \mathbb{R}^N for saliency maps or $2^{\{1, \dots, N\}}$ for set-valued explanations), the *Uncertainty-Aware Relevance Attribution Operator* is

$$\mathcal{U}_\Phi(x) = \Phi(p_{q_\phi}(\cdot | x, \mathcal{D})). \quad (20)$$

The finite-sample approximation of $\mathcal{U}_\Phi(x)$ using S i.i.d. draws $\theta^{(s)} \sim q_\phi$ is denoted $\hat{\mathcal{U}}_\Phi(x)$.

Table 1 lists concrete choices of Φ . For i.i.d. samples $\{\theta^{(s)}\}_{s=1}^S \sim q_\phi$, define

$$R^{(s)}(x) = \tau_x(\theta^{(s)}), \quad \bar{R}(x) = \frac{1}{S} \sum_{s=1}^S R^{(s)}(x).$$

For compactness, write $r_{s,n} = R^{(s)}(x)[n]$, $\bar{R}_n = \bar{R}(x)[n]$, and, for $S > 1$,

$$\hat{s}_n^2 = \frac{1}{S-1} \sum_{s=1}^S (r_{s,n} - \bar{R}_n)^2.$$

The threshold $\delta > 0$ is a relevance cutoff, $\eta \in [0, 1]$ is a posterior agreement level, and $\kappa > 0$ is a small stabilising constant. The set-valued definitions use positive relevance. For unsigned saliency, replace $r_{s,n} > \delta$ by $|r_{s,n}| > \delta$.

Table 1: Instantiations of the UA-RAO, their formulas, and the type of uncertainty conveyed.

Instantiation	Formula	Uncertainty conveyed
Mean explanation	$\widehat{\mathcal{U}}^{\text{mean}}(x) = \bar{R}(x)$	Posterior central tendency of the attribution map; averages over parameter realisations rather than relying on a single model.
Variance map	$\widehat{\mathcal{U}}^{\text{var}}(x)[n] = \hat{s}_n^2$	Feature-wise dispersion of relevance across posterior samples.
α -quantile explanation	$\widehat{\mathcal{U}}^\alpha(x)[n] = r_{([\alpha S]),n}$, where $r_{(1),n} \leq \dots \leq r_{(S),n}$ are the order statistics of $\{r_{1,n}, \dots, r_{S,n}\}$ and $\alpha \in (0, 1)$.	Confidence-indexed localisation. At coordinate n , at least a fraction $1-\alpha$ of posterior samples exceed $r_{([\alpha S]),n}$ by construction of the order statistics. Small α retains only features with consistently high relevance across posterior samples, and large α includes features that are highly relevant in at least some posterior samples.
Coefficient of variation	$\widehat{\mathcal{U}}^{\text{cv}}(x)[n] = \frac{\hat{s}_n}{ \bar{R}_n + \kappa}$	Relative attribution dispersion; most interpretable on features whose mean relevance is not negligible.
Union-type explanation	$\widehat{\rho}_n^\delta(x) = \frac{1}{S} \sum_{s=1}^S \mathbf{1}\{r_{s,n} > \delta\}$, $\widehat{\mathcal{E}}_{\eta,\delta}^\cup(x) = \{n : \widehat{\rho}_n^\delta(x) \geq \eta\}$, with small η .	Plausible-positive relevance set. The empirical union is recovered by $\eta = 1/S$, but a fixed η avoids excessive dependence on the number of posterior samples.
Intersection-type explanation	$\widehat{\mathcal{E}}_{\eta,\delta}^\cap(x) = \{n : \widehat{\rho}_n^\delta(x) \geq \eta\}$, with η close to 1.	Consensus relevance set. The strict empirical intersection is recovered by $\eta = 1$.

Remark 3.4 (Monte Carlo Consistency of the UA-RAO Estimators). For instantiations of Φ that are expectations of a q_ϕ -integrable function γ , strong consistency $\widehat{\mathcal{U}}_\Phi(x) \xrightarrow{a.s.} \mathcal{U}_\Phi(x)$ follows directly from **Proposition 3.1**. This covers the mean explanation, variance map, and coefficient of variation. For the quantile and set-valued instantiations, consistency follows from the Glivenko–Cantelli theorem applied to the empirical distribution of $\{R^{(s)}(x)\}_{s=1}^S$ [21], provided $p_{q_\phi}(\cdot \mid x, \mathcal{D})$ is non-atomic at the quantile levels of interest.

4. Evaluation Framework

Building on the theoretical guarantees in Section 3, this section defines the evaluation framework for assessing UA-RAO explanations empirically. It specifies the ground-truth disturbance reference, localisation metrics for point explanations, their extension to distributional UA-RAO summaries, and the qualitative visualisation protocol. These definitions are independent of a particular posterior approximation or attribution operator and provide the basis for the experiments in Section 5.

4.1. Ground-Truth Disturbance Segmentation

Quantitative evaluation of any XAI method requires a reference against which explanation quality can be measured. In PQD classification, ground-truth disturbance locations are directly available from the signal generation model, a property that avoids the annotation scarcity which limits XAI evaluation in many other domains [6]. In practice, the observed waveform x is a noisy observation of a disturbed signal,

$$x[n] = x_0[n] + d_x[n] + \sigma[n], \quad n = 1, \dots, N, \quad (21)$$

where $x_0[n]$ is the disturbance-free reference of Eq. (1), $d_x[n]$ is the disturbance component associated with input x , and $\sigma[n]$ represents additive measurement noise. Since $d_x[n]$ is known from the signal generation process, disturbance regions are identified as time indices at which the disturbance component exceeds a prescribed tolerance.

Definition 4.1 (ε -Ground-Truth Disturbance Mask). Let $\varepsilon > 0$ be a threshold representing the minimum meaningful disturbance amplitude. The ε -ground-truth disturbance mask is the binary vector $R_{\text{GT}}(x) \in \{0, 1\}^N$ defined componentwise by

$$R_{\text{GT}}(x)[n] = \begin{cases} 1, & \text{if } |d_x[n]| > \varepsilon, \\ 0, & \text{otherwise,} \end{cases} \quad n = 1, \dots, N, \quad (22)$$

where $R_{\text{GT}}(x)[n] = 1$ indicates that time index n lies within a disturbance region. The set of all disturbance indices is denoted $\mathcal{I}(x) = \{n : R_{\text{GT}}(x)[n] = 1\}$, and its cardinality $L = |\mathcal{I}(x)|$ is the ground-truth disturbance length.

The mask $R_{\text{GT}}(x)$ depends on the disturbance component associated with input x and on the choice of threshold ε . It is independent of the classifier parameters θ and the attribution operator τ_x , and thus constitutes a model-agnostic evaluation reference.

4.2. Localisation Metrics for Point Explanations

For any real-valued saliency map R , two scalar metrics are adopted to measure the alignment between R and $R_{\text{GT}}(x)$. Throughout the quantitative evaluation, real-valued saliency maps are assumed to be nonnegative, i.e., $R \in \mathbb{R}_{\geq 0}^N$. Signed attribution maps are converted to nonnegative relevance maps prior to evaluation.

Relevance Mass Accuracy The RMA of a nonnegative saliency map $R \in \mathbb{R}_{\geq 0}^N$ with respect to $R_{\text{GT}}(x)$ is

$$\text{RMA}(R, x) = \frac{\sum_{n \in \mathcal{I}(x)} R[n]}{\sum_{n=1}^N R[n]}, \quad (23)$$

defined whenever $\sum_{n=1}^N R[n] \neq 0$. RMA measures the proportion of total relevance mass concentrated within the true disturbance region.

Binarized Intersection over Union Let $L = |\mathcal{I}(x)|$ be the ground-truth disturbance length and assume $L > 0$. The *top- L binarisation* of $R \in \mathbb{R}_{\geq 0}^N$ is

$$\hat{R}[n] = \begin{cases} 1, & \text{if } n \in \mathcal{T}_L(R), \\ 0, & \text{otherwise,} \end{cases} \quad (24)$$

where $\mathcal{T}_L(R) \subseteq \{1, \dots, N\}$ denotes the index set of the L largest values of R . Let $\hat{\mathcal{I}}_R = \{n : \hat{R}[n] = 1\} = \mathcal{T}_L(R)$ be the predicted disturbance index set. The IoU score is

$$\text{IoU}(R, x) = \frac{|\hat{\mathcal{I}}_R \cap \mathcal{I}(x)|}{|\hat{\mathcal{I}}_R \cup \mathcal{I}(x)|} \in [0, 1], \quad (25)$$

where $|\cdot|$ denotes set cardinality, the intersection counts positions identified as disturbance by both $\hat{\mathcal{I}}_R$ and $\mathcal{I}(x)$, and the union counts positions identified by either set. A score of 1 indicates perfect overlap.

Remark 4.1 (Consistency of the Top- L Binarization). The top- L binarisation in Eq. (24) enforces that $|\hat{\mathcal{I}}_R| = L = |\mathcal{I}(x)|$, so that the cardinality of the predicted mask matches the ground truth exactly. This eliminates the confounding effect of threshold selection on set size, making IoU a measure of localisation quality rather than of detection scale.

Remark 4.2 (Local XAI and Metric Sensitivity). The disturbance interval $\mathcal{I}(x)$ varies in duration and location across both disturbance categories and individual instances. For long-duration disturbances (e.g., harmonics), $|\mathcal{I}(x)| \approx N$ and high RMA or IoU scores are trivially achievable. For short-duration events (e.g., impulsive transients), $|\mathcal{I}(x)| \ll N$ and both metrics are sensitive discriminators. This instance-dependent structure makes local explanations, i.e., attributions specific to each input x , the natural object of evaluation against $R_{\text{GT}}(x)$.

Under the nonnegativity condition on R and the requirement $\sum_{n=1}^N R[n] \neq 0$, RMA is bounded in $[0, 1]$. IoU is also bounded in $[0, 1]$ for $L > 0$, with larger values indicating better alignment. The two metrics are complementary: RMA is sensitive to the distribution of relevance mass and does not require binarisation, while IoU assesses spatial overlap after binarisation and is insensitive to the magnitude of non-disturbance relevance.

4.3. Distributional Evaluation of UA-RAO Instantiations

The UA-RAO framework produces a family of explanation summaries $\{\widehat{\mathcal{U}}_{\Phi}(x)\}_{\Phi}$ rather than a single saliency map. The localisation metrics are extended to this distributional setting as follows.

Point instantiations. For UA-RAO instantiations that produce nonnegative real-valued relevance maps, specifically the mean explanation $\widehat{\mathcal{U}}^{\text{mean}}$ and the α -quantile explanation $\widehat{\mathcal{U}}^{\alpha}$, the localisation metrics are applied directly:

$$\text{RMA}_{\Phi}(x) = \text{RMA}\left(\widehat{\mathcal{U}}_{\Phi}(x), x\right), \quad \text{IoU}_{\Phi}(x) = \text{IoU}\left(\widehat{\mathcal{U}}_{\Phi}(x), x\right). \quad (26)$$

Set-valued instantiations. The union-type and intersection-type UA-RAO instantiations ($\widehat{\mathcal{E}}_{\eta,\delta}^{\cup}$ and $\widehat{\mathcal{E}}_{\eta,\delta}^{\cap}$ in Table 1) produce binary index sets rather than real-valued maps, requiring set-based precision–recall evaluation rather than RMA or IoU as defined above. Their systematic evaluation across disturbance categories, including sensitivity to the hyperparameters (η, δ) , is deferred to future work.

4.4. Qualitative Evaluation

Qualitative evaluation complements the quantitative metrics through visual inspection of the explanation distribution and its summaries.

Saliency map visualisation. Each real-valued UA-RAO output $\widehat{\mathcal{U}}_{\Phi}(x) \in \mathbb{R}^N$ is normalised to $[0, 1]$ using min–max normalisation prior to display:

$$\widetilde{\mathcal{U}}_{\Phi}(x)[n] = \frac{\widehat{\mathcal{U}}_{\Phi}(x)[n] - \min_{n'} \widehat{\mathcal{U}}_{\Phi}(x)[n']}{\max_{n'} \widehat{\mathcal{U}}_{\Phi}(x)[n'] - \min_{n'} \widehat{\mathcal{U}}_{\Phi}(x)[n']}, \quad (27)$$

and rendered using the `cividis` colormap, which provides a perceptually uniform monotone mapping from $[0, 1]$ to colour and remains legible for colour-vision-deficient readers. When a binary ground-truth mask is displayed, it is rendered separately using a grayscale map. The mean explanation, representative α -quantile explanations, and uncertainty maps such as $\widehat{\mathcal{U}}^{\text{var}}(x)$ or $\widehat{\mathcal{U}}^{\text{cv}}(x)$ are displayed for visual comparison. When evaluated quantitatively, uncertainty maps are treated as diagnostic localisation baselines rather than primary relevance explanations.

5. Experiments

This section applies the evaluation framework from Section 4 to PQD classification experiments. The ground-truth masks, RMA, and IoU metrics defined in Section 4 are evaluated across selected BNN–attribution configurations. The experimental setup is described first, followed by aggregate comparisons, per-class localisation analysis, and qualitative evaluation on both synthetic and real-world data.

5.1. Experimental Setup

The data are generated from the synthetic PQD setting of XPQRS [15]. Each voltage record spans ten cycles of a nominal sinusoidal waveform and includes additive noise and labelled disturbance events. The dataset includes a normal (undisturbed) class. Localisation scores are computed only for the 15 disturbance classes: because a normal waveform has no disturbance component d_x , the ground-truth mask $R_{\text{GT}}(x)$ is identically zero and RMA and IoU are undefined. The evaluation uses five independent test splits with 1500 non-normal instances per split, giving 7500 evaluated waveforms in total. Ground-truth masks are obtained from the clean disturbance reference following Section 4.1.

The classifier is based on the 1D-CNN architecture of Wang and Chen [16]. Because the proposed evaluation requires repeated posterior sampling and repeated local attribution computation for each waveform, we use a

Table 2: Lightweight 1D-CNN architecture.

Layer	Details	Activation
convolution_1	kernel: 1×3 , channel: 8, stride: 1	ReLU
convolution_2	kernel: 1×3 , channel: 8, stride: 1	ReLU
max_pooling_1	kernel: 1×3 , stride: 1	
batch_normalization_1	num_features: 8	
convolution_3	kernel: 1×3 , channel: 16, stride: 1	ReLU
convolution_4	kernel: 1×3 , channel: 16, stride: 1	ReLU
max_pooling_2	kernel: 1×630	
batch_normalization_2	num_features: 16	
flatten_1		
fully_connected_1	num_features: 64	ReLU
batch_normalization_3	num_features: 64	
fully_connected_3	num_features: 16	Softmax

lightweight variant of this 1D-CNN to reduce computational cost while preserving the same convolutional design principle. Specifically, the number of convolutional channels and fully connected units is reduced, and the final temporal aggregation is implemented through a global max-pooling operation over the remaining temporal dimension. The resulting architecture is summarised in Table 2. Unless noted otherwise, attribution is computed for the true class label and signed attributions are converted to absolute relevance.

The evaluation considers three BNN posterior approximations and three post-hoc attribution operators, covering distinct uncertainty estimation and explanation mechanisms. This design allows UA-RAO and its localisation metrics to be assessed across multiple methodological settings rather than a single configuration.

Uncertainty estimation methods:

- *Deep ensembles* [22] train multiple independently initialised networks and use the diversity of their predictions as a non-parametric estimate of predictive uncertainty. They are well-calibrated and robust to distribution shift but incur proportionally higher training cost. Within the UA-RAO framework, each ensemble member serves as a draw from the implicit function-space distribution induced by random initialisation and stochastic optimisation, acting as a proxy for q_ϕ without an explicit parametric posterior.

- *MC Dropout* [23] interprets test-time dropout as approximate Bayesian inference, generating stochastic predictions by randomly masking network units. It is computationally lightweight and imposes no architectural constraint beyond standard dropout layers.
- *Laplace approximation* [24] fits a Gaussian centred at the maximum *a posteriori* (MAP) solution by locally approximating the log-posterior curvature. It operates on a pre-trained network without retraining and can therefore be applied post hoc to any existing classifier.

Attribution operators.

- *Grad-CAM* [25] weights the feature maps of a target convolutional layer by the gradient of the class score with respect to those maps, producing a coarse gradient-based localisation map without modifying the network.
- *LIME* [26] fits a sparse linear surrogate model in the neighbourhood of an input instance via perturbation-based sampling, yielding a local, model-agnostic explanation that requires no access to network gradients.
- *Occlusion* [27] slides a masking window across the input and records the change in class probability at each position, providing a perturbation-based relevance score that requires neither gradient access nor a differentiable model. These three operators represent gradient-based, surrogate-model, and perturbation-based explanation mechanisms. Their structural diversity ensures that the reported UA-RAO results are not artefacts of a single attribution family.

The detailed experimental settings are as follows. Occlusion uses a window length of 60 and stride 1, LIME uses 128 perturbation samples with feature width 16, and Grad-CAM is taken from the fourth convolutional layer. Signed saliency maps (Grad-CAM) are converted to nonnegative relevance via the absolute value before applying RMA and IoU, consistent with the nonnegativity assumption in Section 4.2. Bayesian variants are evaluated with the same attribution operator: the deep ensemble contains five independently trained members, Laplace approximation follows the scalable neural-network Laplace procedure of Ritter et al. [24] with additive damping

Table 3: Comparison of deterministic and Bayesian occlusion explanations using mean UA-RAO. Results are mean \pm standard deviation across five test splits. **Bold** indicates the best value in each metric column.

Method	Accuracy	RMA	IoU
Deterministic baseline	0.9774 \pm 0.0013	0.6132 \pm 0.0031	0.6514 \pm 0.0034
Deep ensemble	0.9813 \pm 0.0021	0.6012 \pm 0.0016	0.6711 \pm 0.0038
Laplace	0.9771 \pm 0.0018	0.6096 \pm 0.0017	0.6518 \pm 0.0011
MC Dropout	0.9769 \pm 0.0020	0.6183 \pm 0.0017	0.6493 \pm 0.0024

Table 4: Comparison of XAI operators using deep ensemble and mean UA-RAO. Results are mean \pm standard deviation across five test splits. **Bold** indicates the best value in each metric column.

XAI operator	RMA	IoU
Grad-CAM	0.7190 \pm 0.0027	0.6232 \pm 0.0022
LIME	0.7476 \pm 0.0234	0.6365 \pm 0.0017
Occlusion	0.6012 \pm 0.0016	0.6711 \pm 0.0038

10^2 and multiplicative scaling 1.75×10^{10} , where the damping coefficient regularises near-zero Hessian eigenvalues and the multiplicative scaling adjusts the posterior variance to match the empirical predictive confidence on the validation set following the post-hoc tuning procedure of [24]. MC Dropout uses dropout probability 0.2. Laplace approximation and MC Dropout each use 20 posterior samples. All numerical values are reported as mean \pm standard deviation over the five test splits.

5.2. Numerical Results and Discussion

Table 3 compares the deterministic occlusion baseline with three Bayesian posterior approximations, each paired with the same occlusion operator and mean UA-RAO summary. The deep ensemble improves macro accuracy from 0.9774 to 0.9813 and IoU from 0.6514 to 0.6711 over the deterministic baseline. MC Dropout obtains the highest RMA, indicating that it concentrates a slightly larger fraction of relevance mass inside the ground-truth region, but its IoU is lower than that of the deep ensemble. Since IoU directly measures localisation after matching the disturbance length, the deep ensemble achieves the strongest overall balance between predictive accuracy and spatial localisation, and is used as the Bayesian backbone for the remaining exper-

Table 5: Comparison of UA-RAO summaries using deep ensemble and occlusion. Results are mean \pm standard deviation across five test splits. **Bold** indicates the best value in each metric column.

UA-RAO summary	RMA	IoU
Mean	0.6012 ± 0.0016	0.6711 ± 0.0038
Variance	0.5831 ± 0.0016	0.5795 ± 0.0024
Coeff. variation	0.6084 ± 0.0026	0.5981 ± 0.0044
5% quantile	0.6228 ± 0.0038	0.6592 ± 0.0026
25% quantile	0.6178 ± 0.0035	0.6632 ± 0.0014
50% quantile	0.6093 ± 0.0030	0.6553 ± 0.0022
75% quantile	0.6044 ± 0.0019	0.6365 ± 0.0039
95% quantile	0.5957 ± 0.0019	0.6487 ± 0.0057

iments. Under **Proposition 3.2**, a better posterior approximation would be expected to induce a more faithful explanation distribution. Although $W_1(p(\theta | \mathcal{D}), q_\phi)$ is not directly measurable here, the empirical results suggest that the deep ensemble provides a more useful approximation for localisation in this setting. This can reflect the greater function-space diversity induced by independent random initialisations, which can provide broader posterior coverage than the more constrained Gaussian approximations used by Laplace and MC Dropout.

Table 4 compares explanation operators while holding the Bayesian backbone fixed to the deep ensemble and the UA-RAO summary fixed to the mean explanation. Because Tables 4 and 5 use the same deep ensemble classifier, predictive accuracy is identical across rows (0.9813 ± 0.0021) and is omitted from these tables. LIME and Grad-CAM yield higher RMA than occlusion, but their IoU scores are lower. This difference reflects the complementary nature of the two metrics: RMA rewards total relevance mass within long disturbance regions, whereas IoU penalises spatial mismatch after top- L binarisation. Occlusion achieves the strongest IoU, which is consistent with its window-removal mechanism and its alignment with temporal disturbance localisation.

Table 5 reports localisation scores across UA-RAO summaries with the deep ensemble and occlusion operator fixed. Among real-valued relevance summaries, the 5% quantile gives the best RMA, suggesting that low-quantile explanations concentrate relevance mass on consistently supported disturbance regions. The mean explanation gives the best IoU, indicating a better

Table 6: Per-class IoU for deterministic and Bayesian occlusion explanations. **Bold** marks the unique row best.

Disturbance	Det.	Deep ens.	Laplace	MC Drop.
Flicker	0.997 ± 0.000	0.997 ± 0.000	0.997 ± 0.000	0.997 ± 0.000
Flicker+Harm.	0.997 ± 0.000	0.998 ± 0.000	0.997 ± 0.000	0.997 ± 0.000
Flicker+Sag	0.997 ± 0.000	0.997 ± 0.000	0.997 ± 0.000	0.998 ± 0.000
Flicker+Swell	0.997 ± 0.000	0.997 ± 0.000	0.997 ± 0.000	0.997 ± 0.000
Harmonics	0.997 ± 0.000	0.997 ± 0.000	0.997 ± 0.000	0.997 ± 0.000
Imp. trans.	0.005 ± 0.005	0.104 ± 0.018	0.006 ± 0.006	0.004 ± 0.003
Interruption	0.112 ± 0.010	0.105 ± 0.018	0.141 ± 0.004	0.163 ± 0.015
Interruption+Harm.	0.997 ± 0.000	0.997 ± 0.000	0.997 ± 0.000	0.998 ± 0.000
Notch	0.010 ± 0.004	0.020 ± 0.002	0.011 ± 0.004	0.007 ± 0.002
Osc. trans.	0.654 ± 0.011	0.601 ± 0.018	0.665 ± 0.016	0.635 ± 0.007
Sag	0.291 ± 0.037	0.364 ± 0.030	0.281 ± 0.034	0.259 ± 0.026
Sag+Harm.	0.997 ± 0.000	0.998 ± 0.000	0.998 ± 0.000	0.998 ± 0.000
Spike	0.106 ± 0.015	0.123 ± 0.015	0.078 ± 0.020	0.034 ± 0.004
Swell	0.618 ± 0.014	0.773 ± 0.010	0.619 ± 0.012	0.659 ± 0.011
Swell+Harm.	0.997 ± 0.000	0.997 ± 0.000	0.997 ± 0.000	0.997 ± 0.000

Table 7: Per-class IoU for XAI operators with deep ensemble mean UA-RAO. **Bold** marks the unique row best.

Disturbance	Grad-CAM	LIME	Occlusion
Flicker	0.997 ± 0.000	0.997 ± 0.000	0.997 ± 0.000
Flicker+Harm.	0.997 ± 0.000	0.997 ± 0.000	0.998 ± 0.000
Flicker+Sag	0.997 ± 0.000	0.997 ± 0.000	0.997 ± 0.000
Flicker+Swell	0.997 ± 0.000	0.997 ± 0.000	0.997 ± 0.000
Harmonics	0.997 ± 0.000	0.997 ± 0.000	0.997 ± 0.000
Imp. trans.	0.101 ± 0.022	0.003 ± 0.004	0.108 ± 0.024
Interruption	0.246 ± 0.015	0.129 ± 0.014	0.105 ± 0.019
Interruption+Harm.	0.997 ± 0.000	0.997 ± 0.000	0.997 ± 0.000
Notch	0.060 ± 0.002	0.019 ± 0.002	0.020 ± 0.002
Osc. trans.	0.329 ± 0.013	0.591 ± 0.013	0.601 ± 0.018
Sag	0.273 ± 0.017	0.318 ± 0.013	0.364 ± 0.030
Sag+Harm.	0.997 ± 0.000	0.997 ± 0.000	0.998 ± 0.000
Spike	0.055 ± 0.001	0.026 ± 0.002	0.126 ± 0.017
Swell	0.308 ± 0.012	0.486 ± 0.028	0.773 ± 0.010
Swell+Harm.	0.997 ± 0.000	0.997 ± 0.000	0.997 ± 0.000

Table 8: Per-class IoU for UA-RAO summaries with deep ensemble occlusion. **Bold** marks the unique row best.

Disturbance	Mean	Var.	Coeff. var.	5%	25%	50%	75%	95%
Flicker	0.997 ± 0.000	0.997 ± 0.000	0.997 ± 0.000	0.997 ± 0.000	0.997 ± 0.000	0.997 ± 0.000	0.997 ± 0.000	0.997 ± 0.000
Flicker+Harm.	0.998 ± 0.000	0.997 ± 0.000	0.997 ± 0.000	0.998 ± 0.000	0.997 ± 0.000	0.997 ± 0.000	0.997 ± 0.000	0.997 ± 0.000
Flicker+Sag	0.997 ± 0.000	0.997 ± 0.000	0.997 ± 0.000	0.997 ± 0.000	0.997 ± 0.000	0.997 ± 0.000	0.997 ± 0.000	0.997 ± 0.000
Flicker+Swell	0.997 ± 0.000	0.997 ± 0.000	0.997 ± 0.000	0.997 ± 0.000	0.997 ± 0.000	0.997 ± 0.000	0.997 ± 0.000	0.997 ± 0.000
Harmonics	0.997 ± 0.000	0.997 ± 0.000	0.997 ± 0.000	0.998 ± 0.000	0.997 ± 0.000	0.997 ± 0.000	0.997 ± 0.000	0.997 ± 0.000
Imp. trans.	0.104 ± 0.018	0.027 ± 0.009	0.036 ± 0.009	0.049 ± 0.012	0.063 ± 0.020	0.061 ± 0.037	0.051 ± 0.016	0.069 ± 0.018
Interruption	0.105 ± 0.018	0.128 ± 0.028	0.332 ± 0.059	0.104 ± 0.016	0.108 ± 0.020	0.108 ± 0.015	0.112 ± 0.017	0.123 ± 0.026
Interruption+Harm.	0.997 ± 0.000	0.997 ± 0.000	0.997 ± 0.000	0.997 ± 0.000	0.997 ± 0.000	0.997 ± 0.000	0.997 ± 0.000	0.997 ± 0.000
Notch	0.020 ± 0.002	0.034 ± 0.004	0.034 ± 0.004	0.009 ± 0.003	0.024 ± 0.004	0.035 ± 0.006	0.025 ± 0.005	0.039 ± 0.009
Osc. trans.	0.601 ± 0.018	0.098 ± 0.013	0.053 ± 0.009	0.638 ± 0.014	0.613 ± 0.018	0.580 ± 0.018	0.547 ± 0.027	0.491 ± 0.028
Sag	0.364 ± 0.030	0.287 ± 0.009	0.398 ± 0.050	0.259 ± 0.028	0.263 ± 0.029	0.271 ± 0.030	0.290 ± 0.025	0.370 ± 0.028
Sag+Harm.	0.998 ± 0.000	0.997 ± 0.000	0.997 ± 0.000	0.997 ± 0.000	0.997 ± 0.000	0.997 ± 0.000	0.998 ± 0.000	0.997 ± 0.000
Spike	0.123 ± 0.015	0.028 ± 0.008	0.027 ± 0.008	0.084 ± 0.015	0.142 ± 0.009	0.192 ± 0.025	0.191 ± 0.018	0.213 ± 0.021
Swell	0.773 ± 0.010	0.115 ± 0.011	0.115 ± 0.011	0.765 ± 0.012	0.759 ± 0.014	0.604 ± 0.035	0.353 ± 0.012	0.449 ± 0.022
Swell+Harm.	0.997 ± 0.000	0.997 ± 0.000	0.997 ± 0.000	0.997 ± 0.000	0.997 ± 0.000	0.997 ± 0.000	0.997 ± 0.000	0.997 ± 0.000

balance between posterior averaging and spatial coverage under top- L binarisation. Variance and coefficient-of-variation maps are weaker at the aggregate level, suggesting that attribution dispersion alone is not generally sufficient as a localisation summary, although it can be informative for specific classes. Section 5.3 examines whether these aggregate trends hold uniformly across disturbance categories or are concentrated in specific event types.

5.3. Per-Class Localisation Analysis

To examine whether the macro-level trends are consistent across disturbance types, Tables 6–8 report per-class IoU scores. The values are computed as mean \pm standard deviation of the class-wise IoU over the five test splits. IoU is used for this per-class comparison because it is applicable to deterministic explanations and real-valued UA-RAO summaries, and directly measures spatial overlap with the ground-truth disturbance interval.

The per-class results partition the disturbance types into distinct performance regimes. Long-duration and composite disturbances, including flicker, harmonics, and harmonic mixtures, achieve IoU scores near unity for nearly all point-valued explanations. These classes occupy a large portion of the waveform or contain persistent harmonic components, so the top- L mask is relatively easy to align with the ground-truth disturbance interval. For these classes, $|\mathcal{I}(x)| \approx N$, so methods assigning relevance broadly across the waveform can obtain near-unity IoU by construction. These ceiling-effect classes therefore provide limited discrimination between methods. Excluding them from macro-level metrics would yield a more informative assessment of localisation performance on challenging events.

For localised but distinctive disturbances, the benefit of Bayesian averaging is class-dependent. The deep ensemble improves the deterministic baseline for sag, spike, and especially swell, while Laplace is strongest for oscillatory transient and MC Dropout is strongest for interruption. This suggests that different posterior approximations emphasise different uncertainty structures. Overall, the deep ensemble provides the most consistent behaviour and the strongest macro IoU (Table 3).

The XAI comparison shows that occlusion is the most reliable operator for temporally localised events. It outperforms Grad-CAM and LIME on impulsive transient, oscillatory transient, sag, spike, and swell. Grad-CAM is strongest for interruption and notch, but its performance is weaker for sag, swell, and oscillatory transient. This supports the use of occlusion as

the default attribution operator for PQD localisation, because it directly measures the effect of removing contiguous waveform segments.

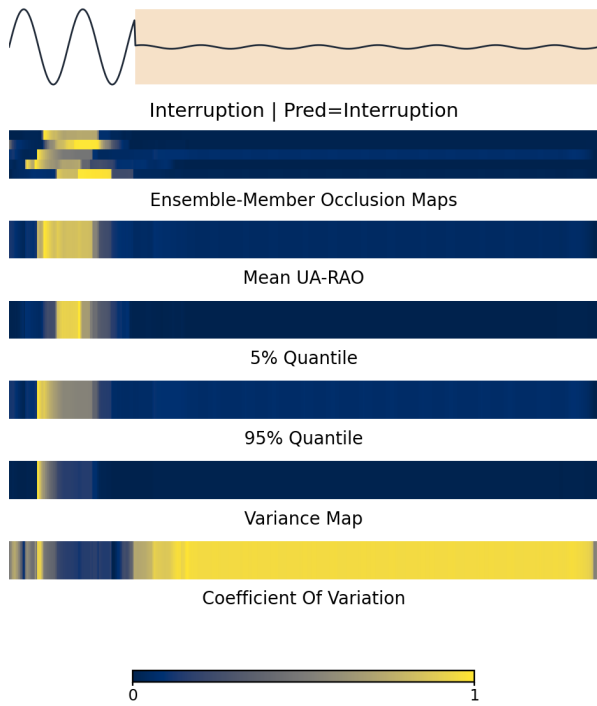
The UA-RAO comparison shows how posterior summaries change localisation behaviour. The 5% quantile improves oscillatory transient relative to the mean explanation, indicating that conservative posterior agreement can sharpen localisation for some transient patterns. Higher quantiles improve notch and spike, where broader posterior support can recover disturbance regions that are only intermittently emphasised.

The coefficient of variation is strongest for interruption and sag, suggesting that attribution dispersion itself can align with disturbance boundaries for these ambiguous classes, although it remains weaker than mean or quantile summaries at the macro level. In terms of waveform structure, interruptions produce an abrupt near-zero amplitude plateau whose onset and recovery create sharp transitions. Ensemble members trained with different random seeds emphasise these edges inconsistently, producing high \hat{U}^{cv} precisely at the disturbance margins. A similar mechanism applies to voltage sags, where the transition regions between nominal and reduced amplitude are the loci of highest inter-member attribution disagreement. For swell, the mean and 5% quantile remain substantially stronger than the higher quantiles, showing that overly inclusive summaries can dilute localisation for distinctive events.

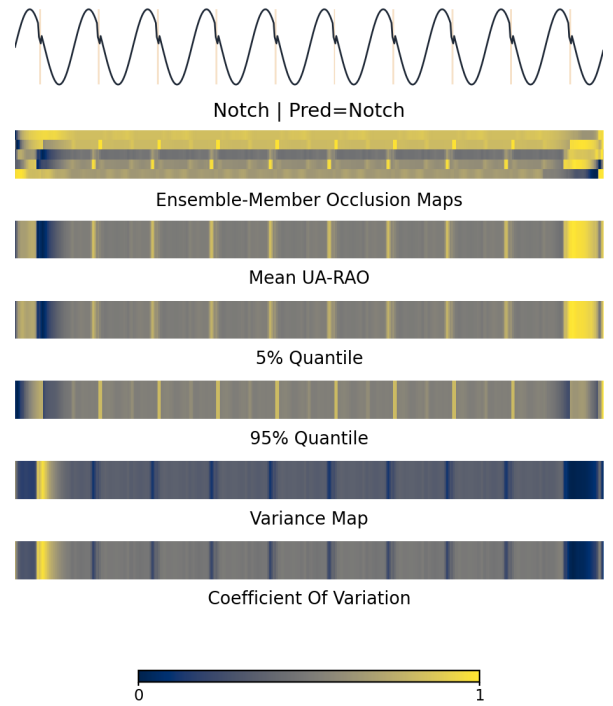
5.4. Qualitative Evaluation on Synthetic Data

Figure 1 provides instance-level visual evidence for the per-class UA-RAO trends summarised in Table 8. The four disturbance types are selected because they represent the most informative cases, excluding ceiling-effect classes, in the per-class evaluation. Together they span four qualitatively distinct uncertainty regimes. Interruption and sag illustrate cases where attribution dispersion, especially the coefficient of variation, is spatially meaningful and can align with disturbance transition regions. Notch represents a short and intermittent disturbance for which broader posterior support, particularly high-quantile summaries, can recover relevance missed by the mean explanation. Swell represents a distinctive amplitude disturbance for which the mean and low-quantile explanations remain concentrated on the true disturbed interval. These examples span ambiguous, localised, intermittent, and distinctive disturbance regimes and collectively illustrate the main per-class trends.

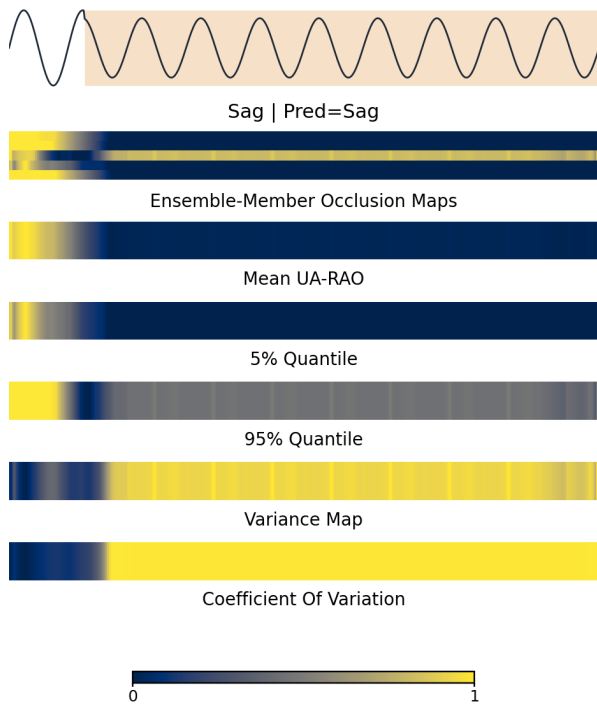
The interruption example in Figure 1a shows that posterior disagreement is concentrated near the disturbance transition region. This explains why the



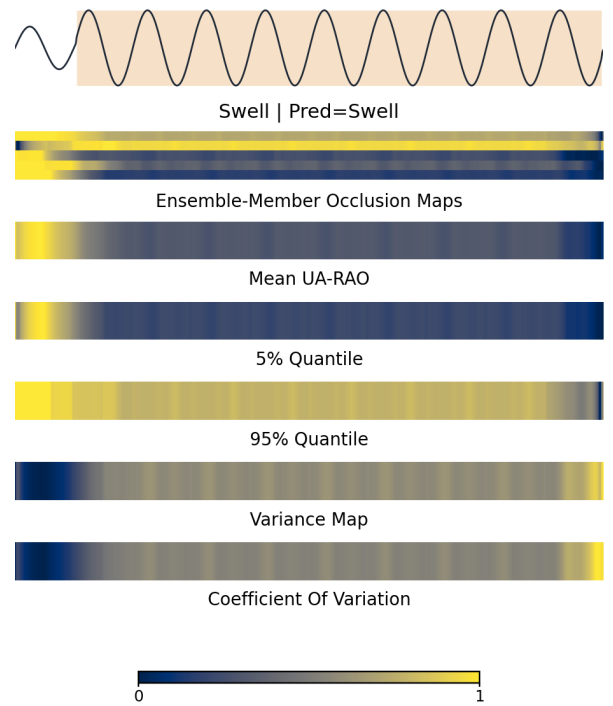
(a) Interruption



(b) Notch



(c) Sag



(d) Swell

Figure 1: Qualitative synthetic examples illustrating the selected per-class UA-RAO behaviour reported in Table 8. Each panel shows the input waveform, ensemble-member occlusion maps, and real-valued UA-RAO summaries, including the mean explanation, quantile explanations, variance map, and coefficient of variation.

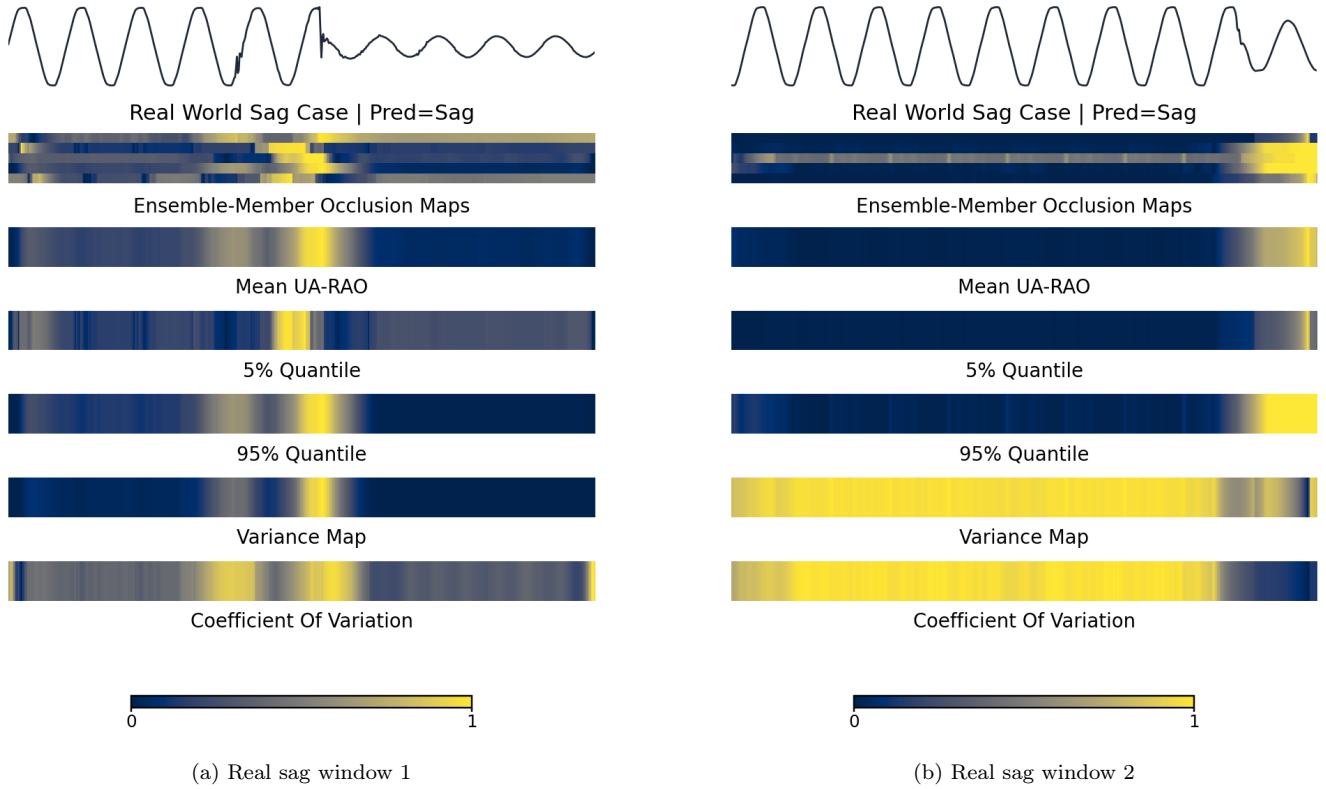


Figure 2: Qualitative real-world sag examples. The two panels show how the selected UA-RAO summaries behave when the synthetic-trained classifier is applied to measured sag events.

coefficient-of-variation summary performs well for interruption in Table 8: although coefficient of variation is not a direct relevance explanation, its high values indicate locations where ensemble members disagree about the temporal evidence for the interruption class. The notch example in Figure 1b illustrates the behaviour of higher quantiles for short and intermittent disturbances. The mean explanation is diffuse, whereas the 95% quantile preserves several narrow high-relevance segments, matching the numerical observation that the high-quantile summary is strongest for notch. The sag example in Figure 1c shows a different uncertainty pattern: variance and coefficient-of-variation maps align with the sag interval and its boundary regions, supporting the interpretation that amplitude-transition regions produce elevated inter-member attribution variability. Finally, the swell example in Figure 1d shows that the mean and 5% quantile remain concentrated over the visually

disturbed interval, while more inclusive summaries become broader. This visually supports the finding that mean and low-quantile summaries are more suitable for distinctive swell events.

5.5. Qualitative Evaluation on Real-World Data

Figure 2 extends the analysis to two of these sag windows using the same deep-ensemble occlusion pipeline, examining whether the qualitative patterns observed in Table 8 persist under real measurement conditions. The real-world data are drawn from the University of Cadiz power network recordings [28], which span five years of continuous measurements at a nominal frequency of 50 Hz sampled at 20 kHz, capturing diverse sag occurrences under operational conditions. For compatibility with the trained 1D-CNN, signals are downsampled to match the synthetic training input length and amplitude-normalised. Ten waveform windows of ten cycles each, containing clearly identifiable sag events, are manually selected and passed directly into the pre-trained model without any fine-tuning.

Both windows are classified as sag, but with different predictive confidence levels. The first exhibits lower sag probability with a competing oscillatory-transient probability, and its attribution maps emphasise a local deformation near the visible waveform change. This suggests that the explanation distribution reflects a more ambiguous real-world decision despite the correct predicted class. The second shows higher sag confidence and more concentrated mean and quantile relevance near the visible sag-related segment. Both cases are consistent with the interpretation from the synthetic sag example: mean and quantile maps provide direct relevance explanations, whereas variance and coefficient-of-variation maps serve as diagnostic summaries of explanation uncertainty under distribution shift.

6. Conclusion

This paper has introduced a unified framework for uncertainty-aware XAI in which the *explanation distribution* is defined as the push-forward measure of a BNN posterior through any Lipschitz-continuous attribution operator, and is summarised by the UA-RAO via mean, variance, quantiles, coefficient of variation, and set-theoretic aggregations. Monte Carlo accessibility and Wasserstein approximation bounds provide the theoretical grounding.

Evaluated on a 15-class power quality disturbance benchmark across three BNN approximations and three attribution operators, deep ensemble poste-

rior averaging improved spatial IoU localisation over the deterministic baseline, and UA-RAO summaries exposed distinct per-class uncertainty patterns. For example, conservative quantile maps sharpened localisation for transient events, while coefficient-of-variation maps aligned with disturbance boundaries for amplitude-modulated classes. Qualitative evaluation on real-world measured signals indicated that these patterns persist beyond the synthetic training distribution. The push-forward formalism and UA-RAO are domain-agnostic: the framework applies to any setting in which a BNN and a Lipschitz-continuous attribution operator can be defined.

Future work includes assessment of architecture sensitivity across larger and more complex network designs, calibration benchmarking of the three BNN approximations using proper scoring rules, and extension to non-Lipschitz attribution operators via smoothing or regularisation.

References

- [1] S. Ali, T. Abuhmed, S. El-Sappagh, K. Muhammad, J. M. Alonso-Moral, R. Confalonieri, R. Guidotti, J. Del Ser, N. Díaz-Rodríguez, F. Herrera, Explainable Artificial Intelligence (XAI): What we know and what is left to attain Trustworthy Artificial Intelligence, *Information Fusion* 99 (2023) 101805.
- [2] W. Samek, G. Montavon, A. Vedaldi, L. K. Hansen, K.-R. Müller (Eds.), *Explainable AI: Interpreting, Explaining and Visualizing Deep Learning*, Vol. 11700 of *Lecture Notes in Artificial Intelligence*, Springer, Cham, 2019.
- [3] European Parliament and Council of the European Union, Regulation (EU) 2016/679 of the European Parliament and of the Council on the Protection of Natural Persons with Regard to the Processing of Personal Data and on the Free Movement of Such Data (General Data Protection Regulation), *Official Journal of the European Union*, L 119, 1–88 (2016).
- [4] M. Haslgrübler, B. Azadi, A. Ferscha, Visual saliency distribution maps for explaining time-series ai models used in continuous production of textile fibers, *Information Fusion* (2025) 103897.
- [5] G. Yang, Q. Ye, J. Xia, Unbox the black-box for the medical explainable ai via multi-modal and multi-centre data fusion: A mini-review, two showcases and beyond, *Information Fusion* 77 (2022) 29–52.

- [6] M. Nauta, J. Trienes, S. Pathak, E. Nguyen, M. Peters, Y. Schmitt, J. Schlötterer, M. Van Keulen, C. Seifert, From anecdotal evidence to quantitative evaluation methods: A systematic review on evaluating Explainable AI, *ACM Computing Surveys* 55 (13s) (2023) 1–42.
- [7] Y. Chen, S. S. Yu, Z. Li, J. K. Eshraghian, C. P. Lim, Interplay between Bayesian neural networks and deep learning: A survey, *Knowledge-Based Systems* 330 (2025) 114438.
- [8] L. Han, X. Zhang, J. Wang, Adaptive probabilistic information fusion under concept drift: A generalized bayesian framework, *Information Fusion* (2025) 104010.
- [9] K. Bykov, M. M.-C. Höhne, K.-R. Müller, S. Nakajima, M. Kloft, How much can i trust you?—quantifying uncertainties in explaining neural networks, *arXiv preprint arXiv:2006.09000* (2020).
- [10] M. Mulye, M. Valdenegro-Toro, Uncertainty quantification for gradient-based explanations in neural networks, in: *Proceedings of the Computer Vision and Pattern Recognition Conference, 2025*, pp. 1752–1760.
- [11] D. Wood, T. Papamarkou, M. Benatan, R. Allmendinger, Model-agnostic variable importance for predictive uncertainty: an entropy-based approach, *Data Mining and Knowledge Discovery* 38 (2024) 4184–4216.
- [12] T. Peltola, Local interpretable model-agnostic explanations of Bayesian predictive models via kullback-leibler projections, *arXiv preprint arXiv:1810.02678* (2018).
- [13] K. Bykov, M. M. Höhne, A. Creosteanu, K. R. Müller, F. Klauschen, S. Nakajima, M. Kloft, Explaining Bayesian neural networks, *Transactions on Machine Learning Research* (2025).
- [14] M. C. A. Clare, M. Sonnewald, R. Lguensat, J. Deshayes, V. Balaji, Explainable Artificial Intelligence for Bayesian Neural Networks: Towards trustworthy predictions of ocean dynamics, *arXiv preprint arXiv:2205.00202* (2022).

- [15] M. U. Khan, S. Aziz, A. Usman, XPQRS: Expert power quality recognition system for sensitive load applications, *Measurement* 216 (2023) 112889.
- [16] S. Wang, H. Chen, A novel deep learning method for the classification of power quality disturbances using deep convolutional neural network, *Applied Energy* 235 (2019) 1126–1140.
- [17] R. Machlev, A. Chachkes, J. Belikov, Y. Beck, Y. Levron, Open source dataset generator for power quality disturbances with deep-learning reference classifiers, *Electric Power Systems Research* 195 (2021) 107152.
- [18] R. Machlev, M. Perl, J. Belikov, K. Y. Levy, Y. Levron, Measuring explainability and trustworthiness of power quality disturbances classifiers using XAI—explainable artificial intelligence, *IEEE Transactions on Industrial Informatics* 18 (8) (2021) 5127–5137.
- [19] V. I. Bogachev, M. A. S. Ruas, *Measure theory*, Vol. 1, Springer, 2007.
- [20] P. Billingsley, *Probability and measure*, John Wiley & Sons, 2017.
- [21] R. Durrett, *Probability: theory and examples*, Vol. 49, Cambridge university press, 2019.
- [22] B. Lakshminarayanan, A. Pritzel, C. Blundell, Simple and scalable predictive uncertainty estimation using deep ensembles, in: *Advances in Neural Information Processing Systems*, Vol. 30, 2017.
- [23] Y. Gal, Z. Ghahramani, Dropout as a Bayesian approximation: Representing model uncertainty in deep learning, in: *Proceedings of the 33rd International Conference on Machine Learning*, 2016, pp. 1050–1059.
- [24] H. Ritter, A. Botev, D. Barber, A scalable laplace approximation for neural networks, in: *6th International Conference on Learning Representations*, 2018.
- [25] R. R. Selvaraju, M. Cogswell, A. Das, R. Vedantam, D. Parikh, D. Batra, Grad-CAM: Visual explanations from deep networks via gradient-based localization, in: *Proceedings of the IEEE International Conference on Computer Vision*, 2017, pp. 618–626.

- [26] M. T. Ribeiro, S. Singh, C. Guestrin, “Why should I trust you?": Explaining the predictions of any classifier, in: Proceedings of the 22nd ACM SIGKDD International Conference on Knowledge Discovery and Data Mining, 2016, pp. 1135–1144.
- [27] M. D. Zeiler, R. Fergus, Visualizing and understanding convolutional networks, in: European Conference on Computer Vision, Springer, 2014, pp. 818–833.
- [28] O. Florencias-Oliveros, M.-J. Espinosa-Gavira, J.-J. González-de-la Rosa, A. Agüera-Pérez, J.-C. Palomares-Salas, J.-M. Sierra-Fernández, Real-life power quality sags, IEEE Dataport, 2017.
URL <https://dx.doi.org/10.21227/H2K88D>